JACS
JOURNAL OF THE AMERICAN CHEMICAL SOCIETY
Article
pubs.acs.org/JACS

Platinum-Modulated Cobalt Nanocatalysts for Low-Temperature Aqueous-Phase Fischer–Tropsch Synthesis

Hang Wang,[†,#] Wu Zhou,[§,∥,#] Jin-Xun Liu,[‡,#] Rui Si,[⊥] Geng Sun,[†] Meng-Qi Zhong,[†] Hai-Yan Su,[‡] Hua-Bo Zhao,[†] Jose A. Rodriguez,[⊥] Stephen J. Pennycook,[∥] Juan-Carlos Idrobo,[∥] Wei-Xue Li,*[,‡] Yuan Kou,*[,†] and Ding Ma*[,†]

[†]College of Chemistry and Molecular Engineering, Peking University, Beijing, 100871, China
[‡]State Key Laboratory of Catalysis, Dalian Institute of Chemical Physics, Chinese Academic of Sciences, Dalian, 116023, China
[§]Department of Physics and Astronomy, Vanderbilt University, Nashville, Tennessee 37235, United States
[∥]Materials Science and Technology Division, Oak Ridge National Laboratory, Oak Ridge, Tennessee 37831, United States
[⊥]Department of Chemistry, Brookhaven National Laboratory, Upton, New York11973, United States

Supporting Information

ABSTRACT: Fischer–Tropsch synthesis (FTS) is an important catalytic process for liquid fuel generation, which converts coal/shale gas/biomass-derived syngas (a mixture of CO and H_2) to oil. While FTS is thermodynamically favored at low temperature, it is desirable to develop a new catalytic system that could allow working at a relatively low reaction temperature. In this article, we present a one-step hydrogenation–reduction route for the synthesis of Pt–Co nanoparticles (NPs) which were found to be excellent catalysts for aqueous-phase FTS at 433 K. Coupling with atomic-resolution scanning transmission electron microscopy (STEM) and theoretical calculations, the outstanding activity is rationalized by the formation of Co overlayer structures on Pt NPs or Pt–Co alloy NPs. The improved energetics and kinetics from the change of the transition states imposed by the lattice mismatch between the two metals are concluded to be the key factors responsible for the dramatically improved FTS performance.

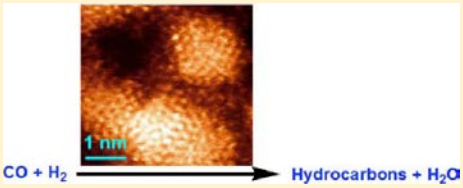

INTRODUCTION

Fischer–Tropsch synthesis (FTS), which converts fossil fuel-based syngas to liquid fuel products over Ru, Co, or Fe catalysts, was used by Germany and South Africa to circumvent oil embargos during the last century. Since it is now possible to use diverse resources, such as coal, biomass, and shale gas as the source for the production of syngas, with the surging consumption of fossil fuels, FTS is once again of essential economic interest as a gas to liquid (GTL) process.[1−8] During the last 80 years, conventional supported and unsupported catalysts have been widely investigated. Research has shown that Ru, Fe, and Co catalysts working in the temperature range of 473–623 K have the best performance.[2−6] Among these catalysts, less expensive Co-based catalysts represent the optimal choice for industrial synthesis of long-chain hydrocarbons due to the higher hydrocarbon productivity, good stability, and commercial availability.[5,6,9]

As the FTS is highly exothermic and thermodynamically favored at low temperature, it is obviously desirable to develop a catalyst system that could facilitate working at low reaction temperature while maintaining excellent catalytic performance. We have recently demonstrated that poly(*N*-vinyl-2-pyrrolidone) (PVP) stabilized Ru nanoparticles (NPs) in aqueous-phase FTS[10] show a 35-fold increase in activity over traditional supported Ru catalyst at an operating temperature of 423 K and a 16-fold increase at only 373 K. As the products of FTS, hydrocarbons, are insoluble in the solvent, water, they can be easily separated from the reaction mixture after the reaction. The reduction of the catalyst particle size, the high dispersion of the NP catalysts, and maintaining the three-dimensional freedom of the particles in water were believed to be the key factors for the significant increase of the catalytic activity at relatively lower temperatures.[11−14] Very recently, Hensen et al. reported that by controlling the reaction parameters, oxygenate selectivity up to 70% can be realized over Ru NP catalyst in aqueous-phase FTS.[15] It was suggested that the reaction temperature strongly affected the relative rates of different termination mechanisms and thus led to unexpectedly high oxygenate selectivity. While the low-temperature aqueous-phase FTS is attractive and has potential for various industrial applications, it is of great importance to find non-noble metal alternatives for the Ru NP catalyst. We began with the conventional FTS element, Fe; however, it was proven that Fe is not stable in aqueous phase and only with the protection of a solvent with strong reduction ability, such as polyethylene glycol,[16] can the low temperature FTS activity be observed on Fe catalysts.

Co-based materials represent another important catalyst for FTS.[17−21] However, traditional Co-based catalysts usually operate at a temperature >473 K in order to get acceptable activity and selectivity, especially for those working under

Received: January 23, 2013
Published: February 21, 2013

   dx.doi.org/10.1021/ja400771a | *J. Am. Chem. Soc.* 2013, 135, 4149–4158

liquid-phase or slurry-phase reaction conditions. Moreover, it is rather challenging to realize FTS in liquid, especially in aqueous phase. Indeed, there have been tremendous endeavors to realize low-temperature FTS over Co-based catalysts in the past decade. For example, Dupont et al.[22] conducted FTS in an ionic liquid [Bmim][NTf_2] with Co NPs as catalysts, and they observed an activity of 0.04 $mol_{CO}{\cdot}mol_{Co}^{-1}{\cdot}h^{-1}$ at 483 K. Yan et al.[23] dispersed Co NPs in squalane and obtained an activity of 1.3 $mol_{CO}{\cdot}mol_{Co}^{-1}{\cdot}h^{-1}$ at 473 K. Fan et al.[16] prepared Co NPs by the $NaBH_4$ reduction method, but the obtained Co NPs show very poor performance in aqueous-phase FTS. Until now, however, there are no reports on the successful construction of a Co-based FTS catalyst system operating at relatively low reaction temperature. Therefore, it is important to improve the activity of Co-based aqueous-phase FTS catalysts at lower temperatures.

It is well documented that the addition of a small amount of noble metals into the transition-metal catalysts may greatly promote the catalytic activity of the latter. For example, the gas-phase FTS performance of Co-based catalysts can be improved greatly by the addition of small amount of Pt, Ru, or Re.[24−27] The noble metals added were thought to facilitate the reduction of cobalt oxide to the active metal state or help to stabilize the metallic Co species through hydrogen spillover and hence accelerate the FTS rates.[5] Besides the reported reduction−improvement effect, it is interesting to know whether those bimetallic catalysts could activate the reactants/intermediates more efficiently because of the altered electronic properties and geometrical structures.[28−34] For the bimetallic catalysts, depending on the preparation and reaction conditions, the two components may form distinct structural motifs, such as an alloy[30,34] or core−shell[31,33−35] structure (both in metallic states) or metal/metal oxide interfaces.[36] How the two metal components interact with each other may affect significantly the reaction performance.

In this work, we report a new hydrogen-reduction route, a Pt seed method, for the aqueous one-step synthesis of Pt−Co bimetallic NP catalysts. The obtained bimetallic Pt−Co NP catalysts have exceptional high aqueous-phase FTS activity at low reaction temperature (433 K). The structure of the bimetallic catalysts was characterized in detail by X-ray absorption fine structure (XAFS) and aberration-corrected scanning transmission electron microscopy (STEM). Various structures, including monometallic (Co or Pt) particles, Co particles with single Pt atoms on the surface, and Co layers decorated on Pt or Pt−Co alloy particles, were observed. Based on density functional theory (DFT) calculations, it is found that the outstanding activity comes from the formation of strained Co layers on Pt or Pt−Co alloy particles, which improve the overall energetics and kinetics by forming favorable transition states (TSs) due to the lattice expansion of the supported Co layers.

EXPERIMENTAL SECTION

Preparation of the Catalysts. Scheme 1 shows the general protocol for the fabrication of Pt−Co bimetallic NPs by one-step hydrogen reduction. In a typical experiment, 0.586 g (2.0×10^{-3} mol) $Co(acac)_2{\cdot}2H_2O$ and 0.084 g (2.0×10^{-4} mol) K_2PtCl_4 are dissolved in 40 mL water containing 2.2 g (2.0×10^{-2} mol) PVP. The mixture was placed in a stainless steel autoclave and treated with 2.0 MPa H_2 at 333 K for 4 h. The obtained material is a black colloidal solution. The as-prepared NPs are termed 10% Pt−Co NPs (analogous procedures are used to form x% Pt−Co NPs). It was believed that the rapidly formed Pt seeds catalyzed the hydrogenation of the carbonyl groups of

Scheme 1. Illustration of One-Step Hydrogen Reduction of Pt−Co Bimetallic NPs

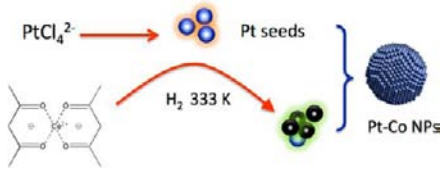

cobalt acetylacetone at a mild temperature, resulting in the simultaneous formation of the Pt−Co bimetallic NPs. As a control, we synthesized Pt NPs in the autoclave by the hydrogen-reduction method first, and then Co precursors (Co/Pt = 10:1) were added. The autoclave was sealed with 2.0 MPa hydrogen, and the reduction/nucleation process was conducted at 333 K for 4 h to obtain 10% Pt−Co−S NPs (hydrogen-sequence-reduction method). As-prepared NPs are magnetically separable (Figures S1 and S2). Pure Co NPs were prepared by the $NaBH_4$ reduction method.[37] Typically, 0.500 g (2.0×10^{-3} mol) $Co(OAc)_2{\cdot}4H_2O$ was dissolved in 20 mL water containing 2.2 g (2.0×10^{-2} mol) PVP. Then 0.4 g (1×10^{-2} mol) $NaBH_4$ was added quickly under vigorous stirring. The mixture turned from red to black immediately, suggesting the formation of Co NPs. Subsequently, the NPs were separated by a magnet and washed with nitrogen-saturated water two times to get Co−$NaBH_4$ NPs. The NPs were then dispersed in 40 mL water containing 2.2 g (2.0×10^{-2} mol) PVP for subsequent FTS reaction. 10% Pt−Co−$NaBH_4$ was prepared by a similar procedure except 0.084 g (2.0×10^{-4} mol) K_2PtCl_4 was added together with $Co(OAc)_2{\cdot}4H_2O$ in the beginning of the synthesis.

Catalytic Performance Testing. In a typical experiment, the freshly prepared catalyst (2.0×10^{-3} mol, in 40 mL water) was placed in a 140 mL stainless steel autoclave. The reactor was purged three times with N_2 (99.99%) and was then sealed with 3.0 MPa syngas with $CO{:}H_2{:}Ar$ = 32:64:4. FTS performance was measured at designated temperatures under stirring (800 r/min) until the total pressure decreased by about 1−1.5 MPa (corresponding to a CO conversion of about 30−50%). Except for the cases of very slow reaction rates, the reaction time required was in the range of 8−24 h. After reaction, the autoclave was cooled down to room temperature, and the products were collected and analyzed. After reaction, the autoclave was linked with gas chromatography (GC) to give a full analysis of the gas products. Porapark Q and 5A packed column with thermal conductivity detector was used to analyze CO_2, CO, Ar, H_2, and CH_4. HP-AL/M column with flame ionization detector (FID) was used to analyze hydrocarbons in the gas phase. Twenty mL cyclohexane was injected into the autoclave through a 20 mL syringe with 20 μL decalin (18.0 mg) as the internal standard. The products were analyzed immediately by Agilent 6820 GC. HP-5 column with FID was used to analyze products in the upper phase (mainly alkanes and olefins, Figure S3). HP-INNOWAX column with FID was used to analyze products in the aqueous phase (no obvious products detected). The calculated carbon balance for a normal FTS analysis is >85%. The products were also qualitatively analyzed by Agilent 7890 GC-5975 MS with HP-5 MS and HP-INNOWAX MS columns.

Characterization. Transmission electron microscopy (TEM) measurements were carried out on a Tecnai F-30 electron microscope operated at 300 kV. The NPs were diluted with deionized water (~0.01 $mol{\cdot}L^{-1}$) and dispersed by ultrasonication for ~15 min. Then one drop of solution was placed on a copper grid coated with a carbon film. The average particle sizes and distributions of the NPs were determined from more than 200 particles for each sample. STEM imaging and spectroscopy analysis were performed on an aberration-corrected Nion UltraSTEM-100 operating at 60 and 100 kV.[38] The convergence semiangle for the incident probe is 31 mrad. Annular dark-field (ADF) images are collected from a half-angle range of ~86−200 mrad. Electron energy loss spectroscopy (EELS) was performed using a Gatan Enfina spectrometer, with a collection semi-angle of 48 mrad. The ADF images presented in this manuscript are low-pass filtered in order to reduce the random noise in the images. Co K and

dx.doi.org/10.1021/ja400771a | J. Am. Chem. Soc. 2013, 135, 4149−4158

Table 1. Catalytic Performances of Various Catalysts[a]

		selectivity (wt%)						
entry	catalysts	CH_4	CO_2	C_{2-4}	C_{5-12}	C_{13-20}	C_{21+}	activity[b] ($mol_{CO}·mol_{Co}^{-1}·h^{-1}$)
1	blank	–	–	–	–	–	–	0
2[c]	Pt NPs	0	100	0	0	0	0	0[d]
3	5% Pt–Co NPs	10	2	17	48	20	3	0.60
4	10% Pt–Co NPs	11	2	17	49	19	2	1.1
5	10% Pt–Co–S NPs	21	38	19	16	6	0	0.10
6	Co–$NaBH_4$ NPs	33	5	41	19	2	0	0.09
7	10% Pt–Co $NaBH_4$ NPs	36	10	32	20	2	0	0.15

[a]Reaction were conducted at 160 °C, $CO/H_2/Ar$ = 32/64/4 (initial pressure = 3.0 MPa). [b]CO_2 not included when calculating the activity. [c]Reduction of K_2PtCl_4 by H_2 at 333 K. [d]Activity of WGSR is 0.44 $mol_{CO}·mol_{Pt}^{-1}·h^{-1}$.

Pt L_{III} edge X-ray absorption fine structure (XAFS) spectra were collected at beamline X19A of the National Synchrotron Light Source at Brookhaven National Laboratory. The sample was mounted onto an adhesive Kapton tape. The XAS spectra were taken repeatedly in the "transmission mode". The monochromator was detuned 35% for Co and 20% for Pt in order to reduce the amount of higher harmonics in the beam. The photon energy was calibrated for each scan with the first inflection point of the Co K (7709 eV) and Pt L_{III} (11564 eV) edge in Co and Pt metal foils, respectively. Extended XAFS (EXAFS) data have been analyzed using the Athena and Artimis programs.[39]

Calculations. DFT spin-polarized calculations have been performed using Vienna Ab Initio Simulation Package (VASP).[40] Throughout the calculations, projector augmented wave (PAW)[41] potentials and the generalized gradient approximation with the Perdew–Burke–Ernzerhof (PBE) exchange–correlation functionals were adopted.[42] The planewave cutoff energy was 400 eV, and the energy and force convergence were 1×10^{-4} eV and 0.02 eV/Å, respectively. Monkhorst–Pack *k*-points sampling of 8 × 8 × 8 was applied for calculating the crystal parameters of bulk Pt and Co with face-centered cubic (fcc) crystal structures, and calculated lattice constants 3.98 and 3.52 Å are used. For Pt_3Co, the optimized lattice constant is 3.89 Å.

The (111) surface was simulated by a four-layer slab, whereas the vicinal (311) surface observed by STEM was simulated by a four equivalent (111) layer slabs. For 1 ML Co/Pt(111), 2 ML Co/Pt(111), and 2 ML Co/Pt(311), the top-most surface Pt atoms were replaced by 1 or 2 ML Co atoms. To construct 1 ML $Co/Pt_3Co(111)$, the top-most surface layer of a five layer $Pt_3Co(111)$ slab was replaced by Co atoms. For Co(311) and 2 ML Co/Pt(311) surfaces, four bottom layers were fixed, whereas for the other surfaces the bottom two layers were fixed. A p(3 × 3) unit cell was used for the (111) surface, while p(2 × 2) unit cell was applied for the stepped (311) surface. The single Co atom decorated Pt(111) surface, labeled as Co1@Pt(111), was simulated by substituting one top-most Pt atom of the Pt(111) surface by a single Co atom. Pt1@Co(111) and Pt1@Co(311) systems were modeled similarly. We used Monkhorst–Pack mesh *k*-points of 5 × 5 × 1 for Co(311) and 2 ML Co/Pt(311) surfaces, 3 × 3 × 1 for 1 ML $Co/Pt_3Co(111)$, and 4 × 4 × 1 for the other (111) surfaces. The vacuum region along the *z* direction was 15 Å at least, and dipole correction was adopted.

Force reversed method[43] was used to determine the TSs, and a force tolerance of 0.03 eV/Å was utilized without the zero point correction. We also searched the TSs of some of the minimum-energy reaction pathways by using the climbing image nudged elastic band method.[44] For the initial and final states, we adopt the separate adsorption of the species involved in the reactions.

RESULTS AND DISCUSSION

Catalytic Performance. The FTS was conducted in aqueous phase at a relatively low temperature of 433 K. As shown in Table 1, without using catalysts, no activity was observed by GC over a 4 h run (Table 1, entry 1). No activity toward hydrocarbon formation was observed over pure Pt NPs (entry 2). Instead, the water–gas shift reaction (WGSR) occurred, which suggests that pure Pt NP catalysts are not active for FTS but are good catalysts for the WGSR, as is well-known for the case of pure Pt NPs.[45] When using pure Co NP catalysts prepared by the $NaBH_4$ reduction method (Table 1, entry 6), the formation of hydrocarbons was detected at 433 K but with poor activity (0.09 $mol_{CO}·mol_{Co}^{-1}·h^{-1}$). At the same time, high methane formation rate and relatively low selectivity toward longer-chain hydrocarbons (C_{2-4}, 41%; C_{5+}, 21%) were observed, which is far less than those in the high-temperature gas-phase FTS process.[17−19] However, when a small amount of Pt (molar ratio of Pt:Co = 0.05) was introduced during the one-step hydrogen-reduction preparation, a dramatic change of the catalytic behavior was observed (Table 1, entry 3). The activity increased to 0.6 $mol_{CO}·mol_{Co}^{-1}·h^{-1}$, around 1 order of magnitude higher than that of the pure Co catalyst, even comparable to Co catalysts working at higher reaction temperatures.[17] More importantly, the selectivity toward unwanted products, methane and CO_2, dropped dramatically (methane: 10%; CO_2: 2%), while those toward C_{2-5} and C_{5+} changed to 17% and 70%, respectively. This indicates that the addition of Pt over the Co NPs could greatly improve the reaction rate of the catalysts.

Upon increasing the Pt loading to 10% (entry 4), the activity increased further, whereas the product distribution remained almost unchanged with 70% selectivity toward C_{5+}. The catalyst was very stable. We conducted recycling experiments for five times on 10% Pt–Co NPs catalyst (Figure 1). The activity dropped only slightly in the second run. After that, it kept

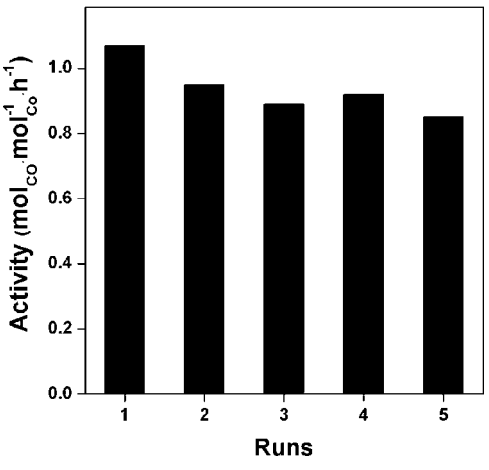

Figure 1. FTS performance of 10% Pt–Co NPs recycling experiments for five times.

dx.doi.org/10.1021/ja400771a | J. Am. Chem. Soc. 2013, 135, 4149−4158

stable during the remaining tests with an activity of 0.85−0.95 $mol_{CO}{\cdot}molCo^{-1}{\cdot}h^{-1}$ (Table S1), which shows that Pt−Co NP catalyst prepared with the one-step hydrogen reduction could be reused. The chain length distribution of the reaction products follows the Anderson−Schulz−Flory statistics, with the growth factor (α) of hydrocarbon products of 0.8 (Figure 2). The product distributions using 10% Pt−Co NPs and Co−

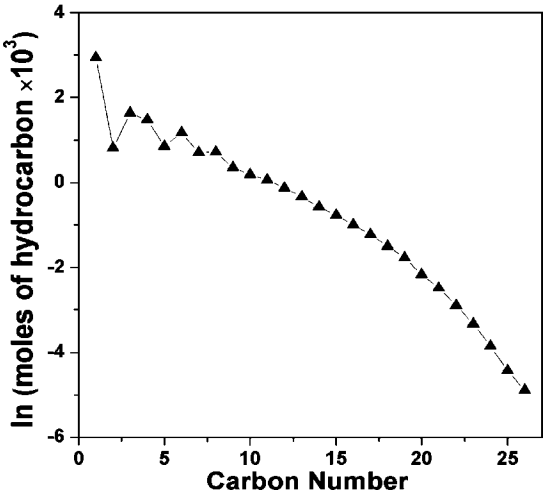

Figure 2. Anderson−Schulz−Flory distribution of products for 10% Pt−Co NP catalyst.

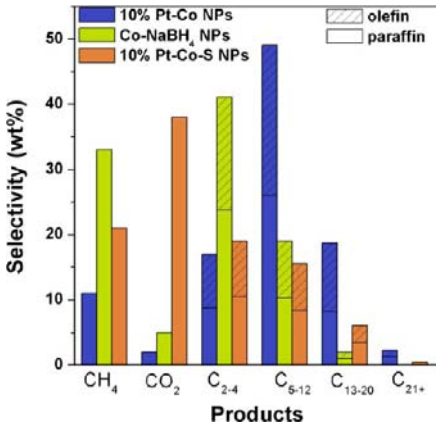

Figure 3. FTS product selectivities for 10% Pt−Co, Co−$NaBH_4$, and 10% Pt−Co−S NPs as catalysts.

$NaBH_4$ NP catalysts in FTS are shown in Figure 3. For 10% Pt−Co NPs, there were only 13% undesired C_1 (CH_4 and CO_2). However, for the Co−$NaBH_4$ NP catalyst, the selectivity toward undesired C_1 products is as high as 38%. Moreover, using the Pt−Co NP catalyst, the more useful olefins take up 49% of the whole C_{2-4} products. For the desired C_{5-12} products, it is clear from Figure 3 that the Pt−Co catalyst has a good selectivity of 49% (with 47% olefins), while it is only 19% (with 46% olefins) over the pure Co NP catalyst. In addition, the share of C_{13-20} products on Pt−Co is 19% while only 2% for Co−$NaBH_4$ NPs. Clearly, beside the possible role of stabilizing the metallic Co species through hydrogen spillover, the addition of Pt with one-step hydrogen-reduction method has a notable effect on increasing the chain growth probability and gives more desired products. Moreover, the relatively low reaction temperature may favor the production of olefins by decreasing the capability of α-hydrogenation in the chain termination step for the Pt−Co NPs catalyst.

It should be mentioned that these highly active Pt−Co bimetallic catalysts were prepared through the one-step hydrogen-reduction method, i.e., adding Pt and Co precursors simultaneously into the synthetic mixture and then reducing with H_2 in a stainless steel autoclave (Scheme 1). The Pt and Co precursors are reduced and nucleated simultaneously. When we prepared the bimetallic sample by the $NaBH_4$ reduction method (Pt−Co−$NaBH_4$ NPs) or by just changing the order of the two metal precursors added in the hydrogen-reduction synthesis process, catalysts with very poor performance were always obtained. As shown in Table 1, entry 7, the 10% Pt−Co−$NaBH_4$ NP catalyst shows activity of 0.15 $mol_{CO}{\cdot}mol_{Co}^{-1}{\cdot}h^{-1}$, while the selectivities toward C_{2-5} and C_{5+} are only 32% and 22%, respectively (Figure 3). For Pt−Co catalysts prepared by the hydrogen sequence reduction method, i.e., 10% Pt−Co−S NPs catalyst, the catalytic performance is similar to that of the Co NP catalyst. It should be noticed that the selectivity toward CO_2 is 38%, suggesting that the water−gas shift activity of this catalyst is emerging, even though not as high as the pure Pt NP catalyst. These results suggest that preparing the bimetallic catalyst by the one-step hydrogen-reduction method is critical for obtaining good catalytic performance for low-temperature aqueous-phase FTS. As the structures of the catalysts with the same composition but different preparation methods may be different, this indicates that the structure of Pt−Co catalysts has a decisive influence on their FTS performance.

Structural Characterization. To identify the origin of the higher activity of the bimetallic catalysts synthesized and the active sites, a series of structural characterizations was carried out. The bimetallic Pt−Co NPs as prepared were first studied by TEM. Two types of particles with different bright-field image contrast were observed in this sample, and their corresponding TEM micrographs and size distributions are shown in Figure 4. It can be found that both low- and high-contrast NPs have a similar average size of 3.4 ± 0.5 and 3.5 ± 0.5 nm with relatively narrow size distribution, respectively. EDX analysis indicates that the low-contrast NPs are composed mainly of Co, whereas the high-contrast NPs are composed mainly of Pt. Similar behavior was found for 5% Pt−Co NPs as prepared (Figure S4). Both the low- and high-contrast NPs give similar average sizes of 3.6 ± 0.7 and 3.6 ± 0.5 nm, although the size distribution is slightly broader in the low-contrast case. This indicates that the different amount of Pt added has little influence on the average size of the catalysts synthesized. After the FT reaction, both the average sizes of low- and high-contrast NPs for 10% Pt−Co NPs (Figure S5) show only slight increases, to 3.6 ± 0.5 and 3.5 ± 0.5 nm. This suggests that the Pt−Co NPs synthesized are rather stable and do not suffer pronounced sintering. For comparison, we show the TEM image for 10% Pt−Co−S NPs in Figure 5. Compared to the 10% Pt−Co NPs, it can be found that the low-contrast particles have a similar average size of 3.3 ± 0.7 nm (versus 3.4 ± 0.5 nm), whereas the high-contrast particles give a smaller average size of 2.9 ± 0.4 nm (versus 3.5 ± 0.5 nm). Although a size-dependent catalytic behavior has been reported on Co-based FTS catalysts,[19] the small size variation observed in the current case cannot explain the huge difference in catalytic performance of the 10% Pt−Co and 10% Pt−Co−S NPs catalysts.

dx.doi.org/10.1021/ja400771a | J. Am. Chem. Soc. 2013, 135, 4149−4158

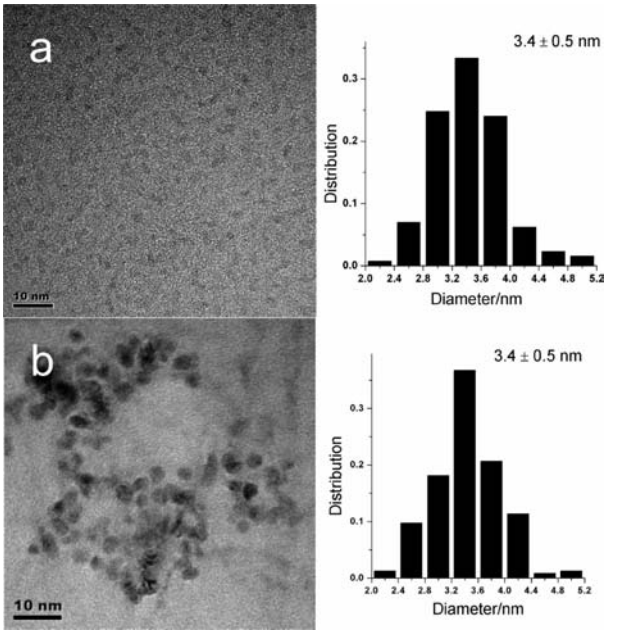

Figure 4. TEM micrographs and size distributions of the (a) low-contrast particles, with size of 3.4 ± 0.5 nm, and (b) high-contrast particles, with size of 3.5 ± 0.5 nm, in the 10% Pt−Co NP catalyst.

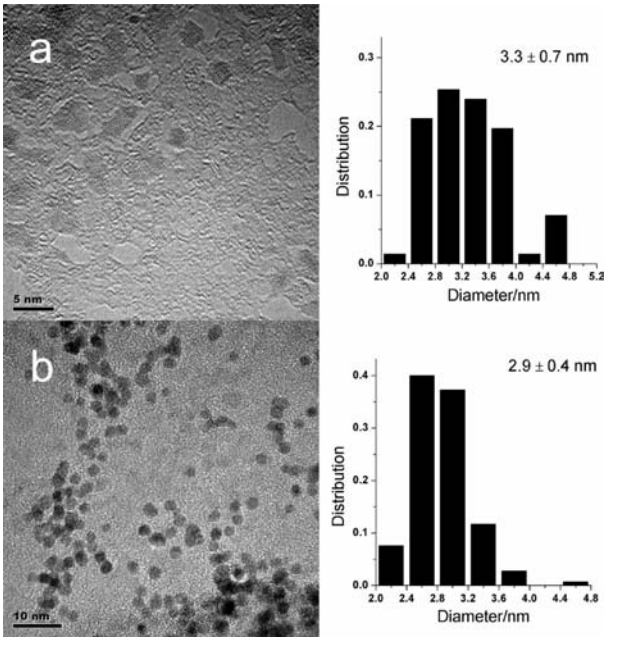

Figure 5. TEM micrographs and size distributions of the (a) low-contrast particles, with size of 3.3 ± 0.7 nm, and (b) high-contrast particles, with size of 2.9 ± 0.4 nm, in the 10% Pt−Co−S NP catalyst.

To get further microscopic structural information of the active Pt−Co NPs, XAFS spectra for as prepared 10% Pt−Co NPs were measured and are shown in Figure 6 (Co K edge). For comparison, the results from 10% Pt−Co−S NPs are also included. For both samples, the normalized X-ray absorption near-edge structure (XANES) spectra (Figure 6a) show four characteristic peaks (A−D), similar to those observed for Co foil. The Fourier transforms of the EXAFS spectra (Figure 6b) indicate a common dominant peak at ∼2.50 Å for both the 10% Pt−Co NPs and 10% Pt−Co−S NPs, a typical bond distance from Co−Co scattering as found in Co foil. The first-shell

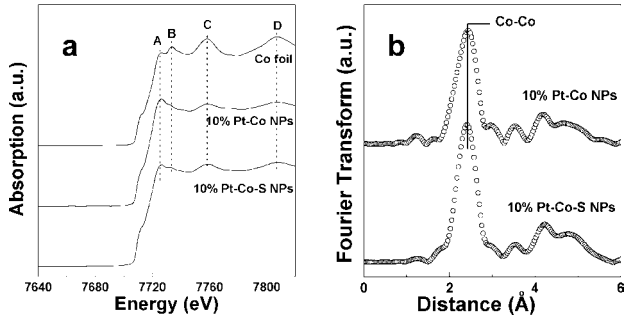

Figure 6. Absorption spectra for different Pt−Co samples collected near the Co K edge: (a) XANES and (b) EXAFS Fourier transforms.

coordination number of Co, $N_{(Co-Co)}$, as well as other structural parameters (e.g., interatomic distance, Debye−Waller factor) can be extracted from EXAFS refinement. The average first-shell coordination number decreased with decreasing particle size. The corresponding $N_{(Co-Co)}$ is 5.4 for 10% Pt−Co NPs and 6.1 for 10% Pt−Co−S NPs. Although $N_{(Co-Co)}$ found here is only half of that for Co foil ($N_{(Co-Co)}$ = 12), our results are in agreement with the results reported by Cheon et al.,[30] where the extracted $N_{(Co-Co)}$ and Co−Co bond distance from Co K edge EXAFS were reported to be 5.2 and 2.49 Å for 4 nm Co particles but 7.1 and 2.49 Å for much larger 7 nm Co particles, respectively. From the Co K edge EXAFS spectra (Figure 6b), there are no pronounced characteristic peaks from Pt−Co coordination found in either 10% Pt−Co or 10% Pt−Co−S NPs. This is due to the fact that Co−Co scattering remains dominant in both samples, which is understandable because only a small amount of Pt (10%) was introduced. Interestingly, at the same experimental condition, we observed a slight smaller $N_{(Co-Co)}$ for 10% Pt−Co NPs (5.4 versus 6.1, 10% Pt−Co−S NPs), although both the catalysts have similar average size (3.4 versus 3.3 nm) for the low-contrast NPs (Co-rich NPs) under TEM. This indicates that the decreased Co−Co coordination for 10% Pt−Co NPs may be due to the Pt−Co coordination, although this is not clearly visible by Co K edge EXAFS experiments.

Table 2. EXAFS Data on the Co K Edge[a]

sample	shell	N	R (Å)	$\Delta\sigma^2$ (Å^2)	ΔE (eV)
Co foil	Co−Co	12	2.49	–	–
10% Pt−Co	Co−Co	5.4	2.50	0.007	0.5
	Co−Pt	–	–	–	
10% Pt−Co−S	Co−Co	6.1	2.49	0.007	0.1
	Co−Pt	–	–	–	

[a]N is the coordination number; $\Delta\sigma^2$ is the change in the Debye−Waller factor value relative to the reference factor; and ΔE is inner potential correction to account for the difference in the inner potential between the sample and the reference.

To better see the Pt−Co and Pt−Pt coordination, XAFS spectra on the Pt L_{III} edge were collected and are shown in Figure 7. A pronounced difference in XANES (Figure 7a) between the 10% Pt−Co and 10% Pt−Co−S NPs can be found. For the former one, after the white lines (peak A), peak B is weak, and peaks C and D shift to slightly higher energies with respect to Pt foil, whereas for the latter one all peaks occur at the similar position as that of Pt foil. A more clear difference can be seen in the Fourier transforms of the EXAFS (Figure 7b). For 10% Pt−Co−S NPs, the dominant feature at around

dx.doi.org/10.1021/ja400771a | J. Am. Chem. Soc. 2013, 135, 4149−4158

Table 3. EXAFS Data on the Pt L_{III} Edge[a]

sample	shell	N	R (Å)	$\Delta\sigma^2$ (Å^2)	ΔE (eV)
Pt foil	Pt−Pt	12	2.76	–	–
10% Pt−Co	Pt−Co	3.6	2.58	0.004	7.3
	Pt−Pt	3.7	2.75	0.004	
10% Pt−Co−S	Pt−Co	1.3	2.57	0.006	8.0
	Pt−Pt	8.6	2.75	0.005	

[a]N is the coordination number; $\Delta\sigma^2$ is the change in the Debye−Waller factor value relative to the reference factor; and ΔE is inner potential correction to account for the difference in the inner potential between the sample and the reference.

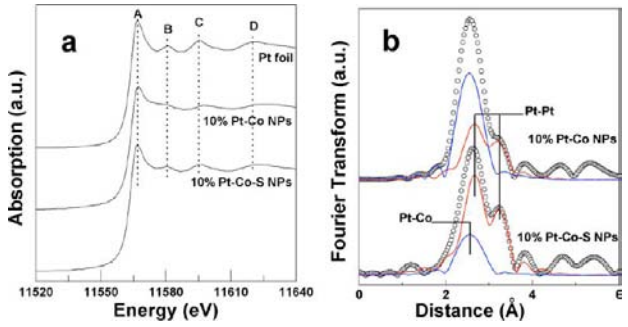

Figure 7. Absorption spectra for different Pt−Co samples collected near the Pt LIII edge: (a) XANES and (b) EXAFS Fourier transforms. The fitting curves for first-shells Pt−Pt (red curve) and Pt−Co (blue curve) are also presented.

2.74 Å from characteristic Pt−Pt scattering is clearly seen. The two large peaks labeled as Pt−Pt are due to a single Pt−Pt path contribution. This splitting is due to Ramsauer−Townsend resonance at a single energy in the backscattering amplitude of Pt.[35,46] The corresponding coordination number $N_{(Pt-Pt)}$ is 8.6, just slightly smaller than that of Pt foil (N = 12) due to the small particle size. In addition, there is a small peak at 2.6 Å from characteristic Pt−Co single scattering with a coordination number of 1.3. For pure Pt particles at around 3 nm, the corresponding $N_{(Pt-Pt)}$ was reported from 8 to 9 in the literature.[47] These results, together with Co K edge EXAFS, suggest that most of the Pt and Co in 10% Pt−Co−S NPs are well separated, possibly staying as discrete Pt and Co NPs. There is less interaction/bonding between Pt and Co. The relatively small coordination of Co ($N_{(Pt-Co)}$ = 1.3) may come from highly dispersed Co atoms over Pt particles or Pt atoms dispersed on Co particles. For 10% Pt−Co NPs, the intensity of the peaks at 2.74 Å for Pt−Pt coordination decreases, while the intensity of the peak at 2.6 Å for Pt−Co scattering increases and becomes even larger than that of Pt−Pt peak. $N_{(Pt-Co)}$ and $N_{(Pt-Pt)}$ for the 10% Pt−Co NPs are 3.7 and 3.6, respectively. The dramatic decrease of Pt−Pt and increase of Pt−Co coordination numbers indicates that Pt in 10% Pt−Co NPs has intensive contact with Co, probably forming Co−Pt bimetallic structures. It should be noted that for interfacially contacted Pt−Co nanostructures, such as a Co−Pt core shell structure, the Pt−Co coordination number at the Pt−Co interface was found to be 2.6.[30] The possibility for the formation of Pt−Co core−shell-like structure may also exist in the 10% Pt−Co NPs catalysts. Although XAFS only gives out statistical/overall structural information, it is clear that the highly active catalyst (10% Pt−Co NPs) has intensive Pt/Co interaction/coordination.

To get more insights into the structures of the bimetallic NPs, aberration-corrected STEM was applied to characterize the structure and composition of the Pt−Co NP catalysts (i.e., 5% and 10% Pt−Co, Figure 8). Since Pt is much heavier, it can

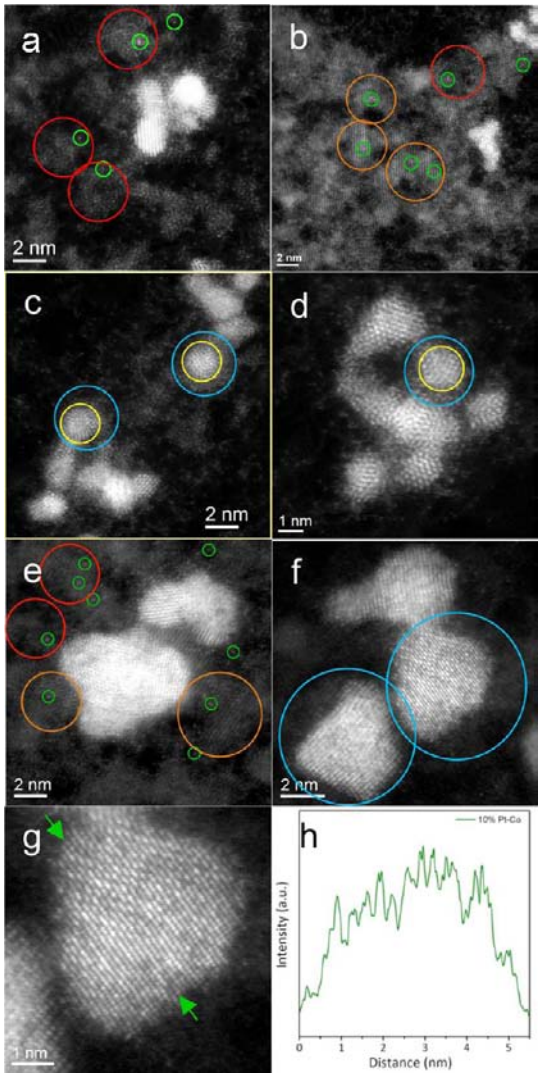

Figure 8. STEM ADF imaging of: (a−d) 5% Pt−Co and (e−h) 10% Pt−Co catalysts. (a−g) ADF images. (h) Intensity line profile taken along the two arrows in (g). Red and orange circles highlight disordered and crystalline Co particles, respectively, decorated by Pt single atoms (green) on the surface. Yellow circles highlight crystalline Pt particles ~2 nm in diameter. The surfaces of the Pt particles are usually decorated by disordered Co layers with lower image contrast (highlighted by the light-blue circles and identified by EELS), with thickness of 1−3 atomic layers. The disordered Co layers on Pt particles are more clearly shown in (d). Some Pt-containing particles in the 10% Pt−Co sample are Pt−Co alloy particles, as shown by the intensity line profile in (g), where abrupt contrast variation between adjacent atomic columns can be observed, suggesting the presence of different amounts of Co in different atomic columns.

be easily distinguished from Co by its higher intensity compared with Co in atomic resolution high-angle annular dark-field (HAADF) images.[48] Besides monometal Pt and Co NPs, Figure 8a−g clearly shows the presence of two additional types of structures in the 5% and 10% Pt−Co samples. They are (i) ordered or disordered Co particles (as identified by EELS) decorated with surface single Pt atoms (highlighted in

dx.doi.org/10.1021/ja400771a | J. Am. Chem. Soc. 2013, 135, 4149−4158

Figure 8a,b,e; denoted as Pt1@Co NPs) and (ii) Pt NPs (2−3 nm, shown in Figure 8c,d) or Pt−Co alloy NPs (4−6 nm, shown in Figure 8f,g) with a few atomic layers (1−3 layers) of Co decoration on the surface, which are termed Co-Layer@Pt NPs or Co-Layer@Pt−Co alloy NPs. The formation of Pt−Co alloy was confirmed by ADF image intensity analysis (Figure 8h) and chemical mapping with EELS (Figure S6). Most of the surface of these Pt or Pt−Co alloy particles consists of Pt {111} and {100} planes, with some small amount of high index planes, like {311} (Figure S7). Importantly, the surface of the Pt and Pt−Co alloy particles in the two active catalyst samples is often observed with a fuzzy low-contrast layer in the ADF images (Figure 8c,d,f), indicating the presence of a surface Co decoration layer in the unoxidized particles. The presence of Co in the surface of the NPs was further supported by EELS mapping (Figure S6), where a skin layer of Co can be seen on the Pt−Co particle surface. Due to the exposure to air during the TEM sample preparation and handling, most of the Co layers were oxidized, making it impossible to determine the precise atomic structure of the Co layers on Pt or Pt−Co alloy NPs in their pristine state. However, it should be noted that the Co surface layers should form during the synthesis instead of being induced by oxidation during *ex-situ* STEM experiment, as previous *ex-situ* electron microscopy studies have already shown that exposure to air would not change the Co and Pt distribution in homogeneous Pt/Co alloy nanostructures.[49−54]

The HAADF-STEM imaging indicates that there is extensive interaction/coordination between Pt and Co in the Pt−Co NP sample, which is in good agreement with the XAFS experiments, where the statistic $N_{(Pt-Co)}$ was calculated to be 3.6. Although atomic resolution STEM observation provides more details about the bimetallic catalysts, the diversity of structures has prevented us from making a direct conclusion of the catalytically active structures. However, the possibility of monometal Pt or Co NPs being the most active species can be ruled out, since the pure Pt NP catalyst only has WGSR activity, and pure Co NP catalysts alone have low FTS activity at 433 K (Table 1, entries 2 and 6). More importantly, for the Pt−Co catalysts with poor FTS activity, the Pt−Co−S NP catalysts, STEM analysis found that it contains mostly pure Pt and pure Co NPs (Figure S8) as well as some Pt1@Co NPs. The pure Pt NPs in the 10% Pt−Co−S sample are highly crystalline and are very similar to those in the pure Pt NP sample (Figure S9). This is in good agreement with the XAFS observation where Pt−Pt coordination dominated the Pt L_{III} edge spectrum. The fact of the common presence of the Pt1@Co NPs in the STEM images of Pt−Co NPs and Pt−Co−S NPs samples with vastly different catalytic performance excludes that Pt1@Co NPs cannot contribute to the different activity. The only difference between the Pt−Co NPs and Pt−Co−S NPs samples is that the former contains Co-layer@Pt NPs and/or Co-layer@Pt−Co alloy NPs structures. Therefore, it is reasonable to conclude that they are responsible for the main FTS activity in the low-temperature aqueous-phase FTS.

DFT Calculations. To shed light on the origin of the higher catalytic activity of the Pt−Co samples and to decisively identify the active structures, we resort here to DFT calculations. For simplicity, we consider here only CO dissociation, which was suggested to be the rate-limiting step for FTS.[55] For reference, we first calculated CO direct dissociation on pure fcc Co, since it is a stable structure at small particle size.[56] Both flat (111) and stepped (311) surfaces observed in experiment were considered to see the structural sensitivity. The calculated potential energy surface of CO direct dissociation on Co(111) and Co(311) is plotted in Figure 9,

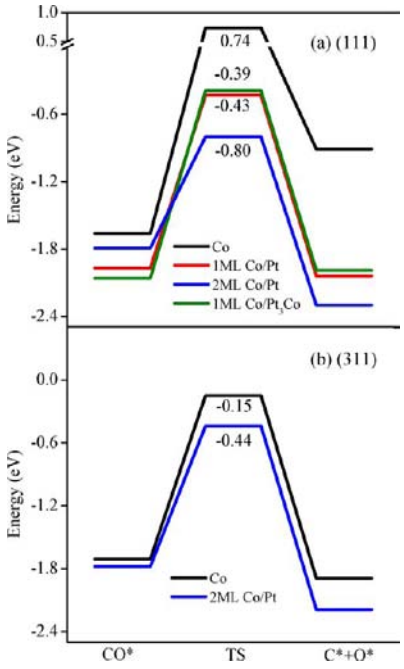

Figure 9. Potential energy surface (in eV) for CO dissociation with respect to CO in gas phase on pristine Co surfaces and Pt supported pseudomorphic epitaxial Co layers. (a) Flat (111) surfaces: Co(111) (black), 1 ML Co/Pt(111) (red), 2 ML Co/Pt(111) (blue), and 1 ML $Co/Pt_3Co(111)$ (green); and (b) stepped (311) surfaces: Co(311) (black) and 2 ML Co/Pt(311) (blue). The energy reference is CO in gas phase, and the calculated barriers are indicated.

Table 4. Calculated CO Adsorption Energy E_{CO} and Barriers E_a with Respect to CO in Gas Phase, Elementary Reaction Energy ΔE from Adsorbed CO to Dissociated C and O, and the Bond Length d (in Å) between C and O at the TS on Various Surfaces Considered[a]

surface	E_{CO}	E_a	ΔE	d
Co(111)	−1.66	0.74	0.75	1.86
Co(311)	−1.71	−0.15	−0.19	2.16
1 ML Co/Pt(111)	−1.97	−0.43	−0.06	1.76
2 ML Co/Pt(111)	−1.79	−0.80	−0.51	1.67
2 ML Co/Pt(311)	−1.78	−0.44	−0.42	1.92
1 ML $Co/Pt_3Co(111)$	−2.04	−0.39	0.05	1.77

[a]The unit for energy is eV.

and details are given in Table 4. The barriers with respect to CO in gas phase (the energy reference defined here is adopted for subsequent discussions unless otherwise specified) are 0.74 and −0.15 eV for Co(111) and Co(311), respectively. The higher activity of the stepped surface agrees well with previous calculations.[57−61] When one surface Co atom of Co(111) or the step Co atom of Co(311) is replaced by a less reactive Pt atom representative of the Co particles decorated with surface single Pt atoms (Pt1@Co NPs), the calculated CO dissociation barriers are at least 0.55 eV higher than those of pure Co counterparts. Moreover, we found that CO dissociation barriers on Pt(111) (1.89 eV) and Pt(311) (0.76 eV) are at least 0.91

dx.doi.org/10.1021/ja400771a | J. Am. Chem. Soc. 2013, 135, 4149−4158

eV higher than those of pure Co counterparts too. Replacing one surface Pt atom of Pt(111) with Co atom (Co1@Pt NPs), the barrier remains 0.37 eV higher than that of pure Co(111). These results (Table S2) exclude the contribution of the Pt1@Co, Co1@Pt, and Pt NPs found by STEM to the higher activity of Pt−Co NPs, a fact nicely in line with the experiments.

We then turn to CO dissociation on Co-Layer@Pt NPs. Although the detailed structure cannot be obtained from STEM, we note that ultrathin Co layers on Pt have been well studied on crystalline surfaces by surface science in the past. It was found that ultrathin Co films on Pt adopt the pseudomorphic epitaxial structure,[62,63] namely, Co layer grown on Pt will adopt the in-plane lattice constant of Pt substrate. We therefore constructed pseudomorphic epitaxial 1 ML Co/Pt(111), 2 ML Co/Pt(111), and 2 ML Co/Pt(311) surfaces to model the Co-layer@Pt NPs. The calculated potential energy surfaces are plotted in Figure 9 (see also Table 4). For 1 ML Co/Pt(111), it was found that the CO binding strength is 0.31 eV stronger than that of pure Co(111), whereas the binding strength with the dissociated C and O is enhanced by 0.60 and 0.52 eV (Table S3, S4 and S5), respectively. This not only improves the CO adsorption but also changes the reaction energy of CO dissociation from endothermic 0.75 eV on Co(111) to exothermic −0.06 eV on 1 ML Co/Pt(111) (Figure 9a). More importantly, the corresponding barrier becomes −0.43 eV, which is 1.17 eV lower than that of the pristine Co(111) and even 0.28 eV lower than that of the more active Co(311). For thicker Co layers on Pt(111), i.e., 2 ML Co/Pt(111), the CO dissociation barrier decreases further to −0.80 eV, and the reaction energy becomes even more exothermic (−0.51 eV). The higher activity of a supported Co layer was also found on a stepped 2 ML Co/Pt(311) surface; compared to the pristine Co(311), the CO dissociation barrier decreases by 0.29 eV, along with improved reaction energy (−0.42 versus −0.19 eV). We also studied the so-called hydrogen-assisted CO dissociation (CO + H → HCO → CH + O).[59,64−66] It was found that the corresponding barrier on 1 ML Co/Pt(111) (1.81 eV with respect to the adsorbed CO and H) is 0.29 eV lower than that of Co(111) (1.52 eV) (Figure S10), whereas on 2 ML Co/Pt(311) the calculated barrier of 1.16 eV is 0.21 eV lower than that of 1.37 eV on Co(311) (Figure S11). These results show that regardless of the surface structures (flat or stepped) and CO dissociation paths (directed or H-assisted), the activity of CO dissociation on epitaxial Co thin layers on Pt has a higher activity than that of the Co catalysts, and this substantiates the Co-Layer@Pt-NPs as an active structure responsible for the higher activity of 5% Pt−Co NPs.

In order to see the influence of Pt−Co alloy, specifically as Co-Layer@Pt−Co alloy NPs observed in 10% Pt−Co NPs, on the activity, we studied the CO dissociation on Pt−Co alloys. For simplification, the Pt−Co alloy was approximated by ordered $Pt_3Co(111)$. On pristine $Pt_3Co(111)$, the top-most surface is composed of three-quarters Pt and one-quarter Co atoms surrounding the Pt atoms. The calculated barrier for CO dissociation on this surface is 1.40 eV (Table S2), 0.66 eV higher than that on Co(111). This surface therefore cannot contribute to the higher activity observed for Pt−Co alloy NPs. This is understandable since there is only one active Co atom involved to break the C−O bond. To study the activity of Co-Layer@Pt−Co alloy NPs observed, similar to the above, we constructed a pseudomorphic epitaxial 1 ML Co on $Pt_3Co(111)$. The calculated CO dissociation barrier on this surface is −0.39 eV, which is already 0.24 eV lower than that of the more active stepped Co(311). This result also substantiates the Co-layer@Pt−Co alloys NPs as an active structure for the higher activity of 10% Pt−Co NPs found in experiment.

The calculations above show that the higher FTS activity for both 5% and 10% Pt−Co samples obtained could be well attributed to the formation of Co-layer structures on Pt NPs or Pt−Co alloy NPs due to the improved energetics and decreased barriers for CO activation. To reveal the origin of this behavior, we note that one distinct structural variation of the supported Co layers is the significant expansion of the in-plane lattice constant, 13% on Pt (111) and 10% on $Pt_3Co(111)$, respectively. The increase of activity from lattice expansion is well documented in the literature.[67] The reason was believed to be an electronic effect, namely, the lattice expansion would induce an upshift of the d-band center of the surface metal atoms, which interacts more strongly with the species involved and stabilizes the TS accordingly. In our case however, compared to the surface metal atoms of Co(111), there are only modest upshifts of the Co 3d center ε_{3d} (<0.08 eV) found for 1 ML Co/Pt(111) and 1 ML Co/$Pt_3Co(111)$. Looking carefully at the spin-resolved projected density of states (PDOS) of 1 ML Co/Pt(111) (Figure S13), it was found that Co ε_{3d} for spin-down states shifts upward by 0.28 eV due to the lattice expansion, whereas Co ε_{3d} for spin-up states shifts downward by 0.09 eV due to the hybridization with Pt underneath. Integrating the spin-resolved PDOS to the Fermi level found that the spin-down states contain less valence electron than the spin-up states (2.51 versus 4.61 *e*, and a corresponding surface Co magnetic moment of 2.1 bohr). These lead to an overall small upshift of Co ε_{3d} of surface Co atoms on Pt. This upshift is too small to account for the change of the energetics and barriers calculated.

The origin of the higher activity of the supported Co layer actually comes from a structural effect, specifically, the formation of a more favorable TS. To approach the TS on Co(111) (Figure 10a), it can be found that C−O bond has to be stretched to 1.86 Å from 1.19 Å at the initial state, and the O atom then sits at the two-fold bridge sites. Whereas for the TS on 1 ML Co/Pt(111) (Figure 10c), the C−O bond is less stretched (1.76 Å) with a lower energy cost for C−O bond

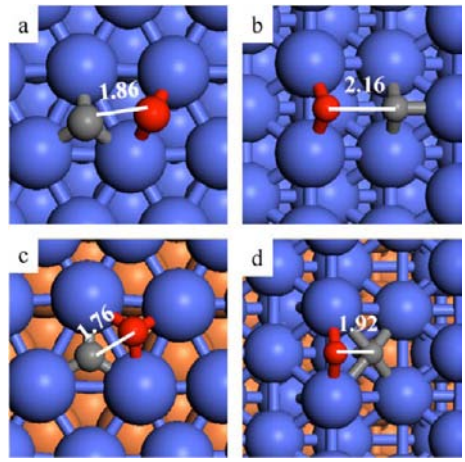

Figure 10. Optimized TSs for CO direct dissociation on: (a) Co(111), (b) Co(311), (c) 1 ML Co/Pt(111), and (d) 2 ML Co/Pt(311). Blue, orange, gray, and red spheres represent Co, Pt, C, and O atoms, respectively. The C−O bond length (Å) at the TS is indicated.

dx.doi.org/10.1021/ja400771a | *J. Am. Chem. Soc.* 2013, 135, 4149−4158

breaking, and the O atom sits at the more favorable three-fold hollow site, leaving more energy gain for oxygen−metal bond making. The exact same changes in the TSs are found on 2 ML Co/Pt(111) and 1 ML Co/Pt_3Co(111) (Figure S14). For the stepped surface, similar structural effects are also found. For instance, for the TS on Co(311) (Figure 10b), the C atom sits at the bridge site with a C−O bond length of 2.16 Å, whereas on 2 ML Co/Pt(311) (Figure 10d), the C atom sits at the more favorable four-fold site with less stretching of C−O bond (1.92 Å). All these structural changes lead to more favorable TSs and facilitate greatly the C−O dissociation on supported Co layers.

CONCLUSIONS

In conclusion, Pt-modulated Co NPs synthesized using a one-step hydrogenation−reduction method were found to be very effective and efficient catalysts for aqueous-phase FTS. The reaction can be operated at 433 K, which is a lower operational temperature than what can be achieved with conventional catalysts. The outstanding activity is rationalized by the formation of Co overlayer structures on Pt NPs or Pt−Co alloy NPs. The improved energetics and kinetics from the change of the TSs imposed by the lattice mismatch between two metals can be used as the basis for the rational design of bimetallic catalysts with low-temperature activities.

ASSOCIATED CONTENT

Supporting Information

Figure S1−15, Table S1−S7. This material is available free of charge via the Internet at http://pubs.acs.org.

AUTHOR INFORMATION

Corresponding Author

dma@pku.edu.cn; yuankou@pku.edu.cn; wxli@dicp.ac.cn

Author Contributions

[#] These authors contributed equally.

Notes

The authors declare no competing financial interest.

ACKNOWLEDGMENTS

This work received financial support from the Natural Science Foundation of China (21222306, 21173009, 20923001, 21225315, 21103164) and 973 Project (2011CB201402, 2013CB933100, 2013CB834603). This research was also supported in part by the U.S. National Science Foundation through grant no. DMR-0938330 (W.Z.); a Wigner Fellowship through the Laboratory Directed Research and Development Program of Oak Ridge National Laboratory, managed by UT-Battelle, LLC, for the U.S. Department of Energy (W.Z.); Oak Ridge National Laboratory's ShaRE User Facility Program (J.-C.I.), which is sponsored by the Office of Basic Energy Sciences, U.S. Department of Energy; and the Office of Basic Energy Sciences, Materials Sciences and Engineering Division, U.S. Department of Energy (S.J.P.). This research carried out in part at the National Synchrotron Light Source at Brookhaven National Laboratory, which is supported by the U.S. Department of Energy, Office of Basic Energy Sciences, under contract DE-AC02-98CH10886. Calculations were carried out at National Supercomputing Center in Tianjin, China.

REFERENCES

(1) (a) Fischer, F.; Tropsch, H. *Brennst.−Chem.* **1923**, *4*, 276−285. (b) Fischer, F.; Tropsch, H. *Brennst.−Chem.* **1926**, *7*, 97−104.

(2) Vannice, M. A. *J. Catal.* **1975**, *37*, 449−461.

(3) Iglesia, E. *Appl. Catal., A* **1997**, *161*, 59−78.

(4) Zhang, Q.; Kang, J.; Wang, Y. *ChemCatChem* **2010**, *2*, 1030−1058.

(5) Khodakov, A. Y.; Chu, W.; Fongarland, P. *Chem. Rev.* **2007**, *107*, 1692−1744.

(6) Schulz, H. *Appl. Catal., A* **1999**, *186*, 3−12.

(7) Iglesia, E.; Soled, S. L.; Baumgartner, J. E.; Reyes, S. C. *J. Catal.* **1995**, *153*, 108−122.

(8) Huber, G. W.; Iborra, S.; Corma, A. *Chem. Rev.* **2006**, *106*, 4044−4098.

(9) Bligaard, T.; Nørskov, J. K.; Dahl, S.; Matthiesen, J.; Christensen, C. H.; Sehested, J. *J. Catal.* **2004**, *224*, 206−217.

(10) Xiao, C. X.; Cai, Z. P.; Wang, T.; Kou, Y.; Yan, N. *Angew. Chem., Int. Ed.* **2008**, *47*, 746−749.

(11) Zhao, D.; Wu, M.; Kou, Y.; Min, E. *Catal. Today* **2002**, *74*, 157−189.

(12) Mu, X. D.; Meng, J. Q.; Li, Z. C.; Kou, Y. *J. Am. Chem. Soc.* **2005**, *127*, 9694−9695.

(13) Yan, N.; Zhao, C.; Luo, C.; Dyson, P. J.; Liu, H.; Kou, Y. *J. Am. Chem. Soc.* **2006**, *128*, 8714−8715.

(14) Wang, T.; Xiao, C. X.; Yan, L.; Xu, L.; Luo, J.; Shou, H.; Kou, Y.; Liu, H. *Chem. Commun.* **2007**, 4375−4377.

(15) Quek, X. Y.; Guan, Y.; van Santen, R. A.; Hensen, E. J. M. *ChemCatChem* **2011**, *3*, 1735−1738.

(16) Fan, X. B.; Tao, Z. Y.; Xiao, C. X.; Liu, F.; Kou, Y. *Green Chem.* **2010**, *12*, 795−797.

(17) Khodakov, A. Y.; Griboval-Constant, A.; Bechara, R.; Zholobenko, V. L. *J. Catal.* **2002**, *206*, 230−241.

(18) Li, J.; Coville, N. J. *Appl. Catal., A* **1999**, *181*, 201−208.

(19) Bezemer, G. L.; Bitter, J. H.; Kuipers, H. P. C. E.; Oosterbeek, H.; Holewijn, J. E.; Xu, X.; Kapteijn, F.; van Dillen, A. J.; De Jong, K. P. *J. Am. Chem. Soc.* **2006**, *128*, 3956−3964.

(20) Zhang, J.; Chen, J.; Ren, J.; Sun, Y. *Appl. Catal., A* **2003**, *243*, 121−133.

(21) Bao, J.; He, J.; Zhang, Y.; Yoneyama, Y.; Tsubaki, N. *Angew. Chem., Int. Ed.* **2008**, *47*, 353−356.

(22) Silva, D. O.; Scholten, J. D.; Gelesky, M. A.; Teixeira, S. R.; Dos Santos, A. C. B.; Souza-Aguiar, E. F.; Dupont, J. *ChemSusChem* **2008**, *1*, 291−294.

(23) Yan, N.; Zhang, J. G.; Tong, Y.; Yao, S.; Xiao, C. X.; Li, Z. C.; Kou, Y. *Chem. Commun.* **2009**, 4423−4425.

(24) Shi, L.; Chen, J.; Fang, K.; Sun, Y. *Fuel* **2008**, *87*, 521−526.

(25) Schanke, D.; Vada, S.; Blekkan, E. A.; Hilmen, A. M.; Hoff, A.; Holmen, A. *J. Catal.* **1995**, *156*, 85−95.

(26) Guczi, L.; Bazin, D.; Kovács, I.; Borkó, L.; Schay, Z.; Lynch, J.; Parent, P.; Lafon, C.; Stefler, G.; Koppány, Z.; Sajó, I. *Top. Catal.* **2002**, *20*, 129−139.

(27) Jacobs, G.; Das, T. K.; Zhang, Y.; Li, J.; Racoillet, G.; Davis, B. H. *Appl. Catal., A* **2002**, *233*, 263−281.

(28) Fu, Q.; Li, W. X.; Yao, Y.; Liu, H.; Su, H. Y.; Ma, D.; Gu, X. K.; Chen, L.; Wang, Z.; Zhang, H.; Wang, B.; Bao, X. *Science* **2010**, *328*, 1141−1144.

(29) Qiao, B.; Wang, A.; Yang, X.; Allard, L. F.; Jiang, Z.; Cui, Y.; Liu, J.; Li, J.; Zhang, T. *Nat. Chem.* **2011**, *3*, 634−641.

(30) Cao, A.; Veser, G. *Nat. Mater.* **2010**, *9*, 75−81.

(31) Wang, D.; Xin, H.; Hovden, R.; Wang, H.; Yu, Y.; Muller, D. A.; DiSalvo, F. J.; Abruña, H. D. *Nat. Mater.* **2013**, *12*, 81−87.

(32) Rodriguez, J. A.; Ma, S.; Liu, P.; Hrbek, J.; Evans, J.; Pérez, M. *Science* **2007**, *318*, 1757−1760.

(33) Alayoglu, S.; Nilekar, A. U.; Mavrikakis, M.; Eichhorn, B. *Nat. Mater.* **2008**, *7*, 333−338.

(34) Xin, H. L.; Mundy, J. A.; Liu, Z.; Cabezas, R.; Hovden, R.; Kourkoutis, L. F.; Zhang, J.; Subramanian, N. P.; Makharia, R.; Wagner, F. T.; Muller, D. A. *Nano Lett.* **2012**, *12* (1), 490−497.

(35) Park, J. I.; Kim, M. G.; Jun, Y. W.; Lee, J. S.; Lee, W. R.; Cheon, J. *J. Am. Chem. Soc.* **2004**, *126*, 9072−9078.

(36) Regan, T. J.; Ohldag, H.; Stamm, C.; Nolting, F.; Lüning, J.; Stöhr, J.; White, R. L. *Phys. Rev. B* **2001**, *64*, 214422.

(37) Cai, Z.; Wang, H.; Xiao, C. X.; Zhong, M. Q.; Ma, D.; Kou, Y. *J. Mol. Catal. A: Chem.* **2010**, *330*, 94−98.
(38) Krivanek, O. L.; Corbin, G. J.; Dellby, N.; Elston, B. F.; Keyse, R. J.; Murfitt, M. F.; Own, C. S.; Szilagyi, Z. S.; Woodruff, J. W. *Ultramicroscopy* **2008**, *108*, 179−195.
(39) (a) Newville, M. *J. Synchrotron Rad.* **2001**, *8*, 322−324. (b) Ravel, B.; Newville, M. *J. Synchrotron Rad.* **2005**, *12*, 537−541.
(40) (a) Kresse, G.; Hafner, J. *Phys. Rev. B* **1993**, *47*, 558−561. (b) Kresse, G.; Furthmüller. *J. Phys. Rev. B* **1996**, *54*, 11169−11186.
(41) (a) Blöchl, P. E. *Phys. Rev. B* **1994**, *50*, 17953−17979. (b) Kresse, G.; Joubert, D. *Phys. Rev. B* **1999**, *59*, 1758−1775.
(42) Perdew, J. P.; Burke, K.; Ernzerhof, M. *Phys. Rev. Lett.* **1996**, *77*, 3865−3868.
(43) Sun, K.; Zhao, Y.; Su, H. Y.; Li, W. X. *Theo. Chem. Acc.* **2012**, *131*, 1118.
(44) Henkelman, G.; Uberuaga, B. P.; Jonsson, H. *J. Chem. Phys.* **2000**, *113*, 9901−9904.
(45) Bunluesin, T.; Gorte, R. J.; Graham, G. W. *Appl. Catal., B* **1998**, *15*, 107−114.
(46) Deng, W. L.; Frenkel, A. I.; Si, R.; Flytzani-Stephanopoulos, M. *J. Phys. Chem. C* **2008**, *112*, 12834−12840.
(47) Lin, C. S.; Khan, M. R.; Lin, S. D. *J. Colloid Interface Sci.* **2006**, *209*, 678−685.
(48) (a) Nellist, P. D. In *Scanning Transmission Electron Microscopy: Imaging and Analysis*; Pennycook, S. J., Nellist, P. D., Eds.; Springer: New York, 2011; pp 91−116. (b) Pennycook, S. J.; Boatner, L. A. *Nature* **1988**, *336*, 565−567.
(49) Oh, J. G.; Oh, H. S.; Lee, W. H.; Kim, H. *J. Mater. Chem.* **2012**, *22*, 15215−15220.
(50) Chen, S.; Ferreira, P. J.; Sheng, W.; Yabuuchi, N.; Allard, L. F.; Shao-Horn, Y. *J. Am. Chem. Soc.* **2008**, *130*, 13818−13819.
(51) Oezaslan, M.; Heggen, M.; Strasser, P. *J. Am. Chem. Soc.* **2012**, *134*, 514−524.
(52) Wang, C.; Chi, M.; Li, D.; van der Vliet, D.; Wang, G.; Lin, Q.; Mitchell, J. F.; More, K. L.; Markovic, N. M.; Stamenkovic, V. R. *ACS Catal.* **2011**, *1*, 1355−1359.
(53) Dubau, L.; Durst, J.; Maillard, F.; Guétaz, L.; Chatenet, M.; André, J.; Rossinot, E. *Electrochim. Acta* **2011**, *56*, 10658−10667.
(54) Alayoglu, S.; Beaumont, S. K.; Zheng, F.; Pushkarev, V. V.; Zheng, H.; Iablokov, V.; Liu, Z.; Guo, J.; Kruse, N.; Somorjai, G. A. *Top. Catal.* **2011**, *54*, 778−785.
(55) Shetty, S.; van Santen, R. A. *Top. Catal.* **2010**, *53*, 969−975.
(56) Kitakami, O.; Sato, H.; Shimada, Y.; Sato, F.; Tanaka, M. *Phys. Rev. B* **1997**, *56*, 13849−13854.
(57) Gong, X. Q.; Raval, R.; Hu, P. *Surf. Sci.* **2004**, *562*, 247−256.
(58) Mavrikakis, M.; Baumer, M.; Freund, H. J.; Nørskov, J. K. *Catal. Lett.* **2002**, *81*, 153−156.
(59) Ciobica, I. M.; van Santen, R. A. *J. Phys. Chem. B* **2003**, *107*, 3808−3812.
(60) Mortensen, J. J.; Morikawa, Y.; Hammer, B.; Nørskov, J. K. *J. Catal.* **1997**, *169*, 85−92.
(61) Mortensen, J. J.; Hammer, B.; Nørskov, J. K. *Phys. Rev. Lett.* **1998**, *80*, 4333−4336.
(62) Valvidares, S. M.; Schroeder, T.; Robach, O.; Quirós, C.; Lee, T. L.; Ferrer, S. *Phys. Rev. B* **2004**, *70*, 224413.
(63) Lundgren, E.; Stanka, B.; Schmid, M.; Varga, P. *Phys. Rev. B* **2000**, *62*, 2843−2851.
(64) Inderwildi, O. R.; Jenkins, S. J.; King, D. A. *J. Phys. Chem. C* **2008**, *112*, 1305−1307.
(65) Morgan, G. A., Jr.; Sorescu, D. C.; Zubkov, T.; Yates, J. T., Jr. *J. Phys. Chem. B* **2004**, *108*, 3614−3624.
(66) van Helden, P.; van den Berg, J.-A.; Ciobîcă, I. M. *Catal. Sci. Tech.* **2012**, *2*, 491−494.
(67) Mavrikakis, M.; Hammer, B.; Nørskov, J. K. *Phys. Rev. Lett.* **1998**, *81*, 2819−2822.